

Article

Refractory High-Entropy HfTaTiNbZr-Based Alloys by Combined Use of Ball Milling and Spark Plasma Sintering: Effect of Milling Intensity

Natalia Shkodich ^{1,2,*}, Alexey Sedegov ¹, Kirill Kuskov ¹ , Sergey Busurin ³, Yury Scheck ², Sergey Vadchenko ² and Dmitry Moskovskikh ¹ 

¹ Center of Functional Nanoceramics, National University of Science and Technology MISIS, Moscow 119049, Russia; sedegov.alex@yandex.ru (A.S.); kkuskov@misis.ru (K.K.); mos@misis.ru (D.M.)

² Merzhanov Institute of Structural Macrokinetics and Materials Science, Russian Academy of Sciences, Chernogolovka, Moscow 142432, Russia; ybsch@mail.ru (Y.S.); vadchenko@ism.ac.ru (S.V.)

³ NTO IRE-POLUS, LCC, Fryazino, Moscow 141190, Russia; bsmihalych@mail.ru

* Correspondence: n.f.shkodich@mail.ru; Tel.: +7-49652-46-299

Received: 1 September 2020; Accepted: 18 September 2020; Published: 20 September 2020



Abstract: For the first time, a powder of refractory body-centered cubic (bcc) HfTaTiNbZr-based high-entropy alloy (RHEA) was prepared by short-term (90 min) high-energy ball milling (HEBM) followed by spark plasma sintering (SPS) at 1300 °C for 10 min and the resultant bulk material was characterized by XRD and SEM/EDX. The material showed ultra-high Vickers hardness (10.7 GPa) and a density of $9.87 \pm 0.18 \text{ g/cm}^3$ (98.7%). Our alloy was found to consist of HfZrTiTaNb-based solid solution with bcc structure as a main phase, a hexagonal closest packed (hcp) Hf/Zr-based solid solution, and Me_2Fe phases (Me = Hf, Zr) as minor admixtures. Principal elements of the HEA phase were uniformly distributed over the bulk of HfTaTiNbZr-based alloy. Similar alloys synthesized without milling or in the case of low-energy ball milling (LEBM, 10 h) consisted of a bcc HEA and a Hf/Zr-rich hcp solid solution; in this case, the Vickers hardness of such alloys was found to have a value of 6.4 GPa and 5.8 GPa, respectively.

Keywords: refractory high-entropy alloys; high-energy ball milling; low-energy ball milling; spark plasma sintering; bcc solid solution

1. Introduction

The classical approach to designing alloys, based on the use of one or two principal elements and minor amounts of other elements added for property enhancement, has been extended by Yeh et al. [1] and Cantor [2], who independently suggested a new concept for the design of multicomponent alloys, termed high-entropy alloys (HEAs). Newly developed HEAs containing at least five components in equiatomic or nearly equiatomic amounts (ranging between 5 and 35 at. %) have received much attention in view of their unique structures and excellent properties [3–9]. The experimental data currently available for more than 400 different HEAs unanimously confirm their unique mechanical, chemical, and electrical properties [10]. The presence of several principal elements in HEAs not only characterizes their composition, but also brings about fundamental physical changes in their configurational entropy, free energy, phase selection, and stability [10,11].

In general, the high-entropy effect in these alloys can greatly reduce the free energy of simple solid-solution phases, especially at high temperatures, thus making chemically ordered intermetallic compounds less competitive owing to the formation of simple solid solutions with a face-centered cubic (fcc), body-centered cubic (bcc), hexagonal closest packed (hcp), or their combinatorial structures [1,2,10].

The formation of solid solutions in HEAs is governed by some thermodynamic parameters such as entropy of mixing (ΔS_{mix}), enthalpy of mixing (ΔH_{mix}), and atomic size difference (δ) [10]. According to [12], HEAs form a simple solid solution when $-22 \leq \Delta H_{\text{mix}} \leq 7$ kJ/mol, $11 \leq \Delta S_{\text{mix}} \leq 19.5$ kJ/mol, and $\delta \leq 8.5\%$.

Moreover, it has been found that a crucial factor, which defines whether or not *fcc* or *bcc* solid solutions appear are formed in HEAs, is the valence electron concentration (VEC) [13]. It has been observed that *bcc* and *fcc* phases are formed for $\text{VEC} < 6.87$ and $\text{VEC} \geq 8.0$, respectively, while both of the phases (i.e., *bcc* + *fcc* mixture) coexist for $6.87 \leq \text{VEC} \leq 8.0$ [13].

The first single-phase CoCrFeMnNi material (also known as the Cantor alloy) has an outstanding combination of properties, such as exceptional resistance to damage and resistance to destruction, especially at cryogenic temperatures [14–16]; high tensile strength and ductility [3–5,17]; superplasticity [5]; and high hardness and strength [3,6,7].

Typical synthesis routes used for the fabrication of traditional alloys can also be applied to the synthesis of HEAs. On the basis of a type of intermixing procedure, existing processing routes can be classified into four categories [18–21]: from liquid phase (arc melting), from solid state (mechanical alloying), from gas phase (sputtering), and from electrodeposition process.

It has been found that different synthesis routes applied to the same starting compositions produce materials with distinctly different microstructure and properties. Thus, the CoCrFeNiTi alloy synthesized by arc melting presents a *fcc*–*bcc* mixture with minor admixture of intermetallic phase [15], while that prepared by mechanical alloying (MA) has a single *fcc* phase [17].

Over the last few years, ever growing attention has been given to HEAs based on refractory metals such as Cr, Hf, Mo, Nb, Ta, Ti, V, W, and Zr [10,22–24]. Meanwhile, these materials having high potential for high-temperature applications still remain to be studied adequately.

Refractory TaNbHfZrTi HEA (*bcc* solid solution, $H_v = 3826$ MPa, $\sigma_{0.2} = 929$ MPa) was produced [23] by arc melting and subsequent consolidation by hot pressing at $T = 1473$ K and $p = 207$ MPa for 3 h. MoNbTaTiV refractory high-entropy alloy with ultra-fine and homogeneous microstructure (*bcc* solid solution) was successfully fabricated by mechanical alloying for 40 h followed by spark plasma sintering (SPS) at 1500–1700 °C [25].

Mechanical alloying (MA) is a well-known solid-state, non-equilibrium, top-down approach for the fabrication of nanocrystalline materials. It involves milling elemental powders to achieve mixing on an atomic scale. This technique has been successfully applied to produce a variety of materials, like intermetallics, ordered compounds, solid-solution alloys, amorphous structures, quasi-crystalline phases, and nanocomposites [26–29]. In addition to nanoscale processing, MA also takes advantage of extended solubility of solids even in immiscible systems [26,30]. This is attributed to elevated diffusion rates arising as a result of a nanosize of starting powder blends. Besides increased configurational entropy, MA imparts enhanced stability to solid-solution phases in HEAs. The first synthesis of HEAs by MA is credited to Varalakshmi et al. [31], who prepared nanocrystalline AlCrCuFeTiZn alloy back in 2008. Since then, MA has been progressively used to synthesize nanocrystalline HEAs, as evidenced by a growing number of publications on mechanically alloyed HEAs. Most solid-solution phases in HEAs form within 15–40 h of milling. Prolonged milling hours are often used for the production of amorphous HEAs [27].

For consolidation of HEAs powders, conventional sintering methods are often used, which include vacuum hot pressing sintering, microwave sintering, and hot isostatic pressing. Among these, a highly promising technique for sintering and production of HEA materials is spark plasma sintering (SPS) [32–34]. The main difference between SPS and conventional hot pressing is that, in SPS, the current is applied as many pulses over very short times (less than milliseconds (ms)) instead of one single pulse for a long time. As with most methods where pressure and temperature are applied simultaneously, both pressure and temperature are lower than would be required if applying them in subsequent steps. This means that lower sintering temperatures and shorter holding times are required, and as a result, less grain growth and better properties can be obtained [33,35].

An equiatomic WNbMoTaV high entropy alloy (HEA) with a *bcc* structure was first fabricated by the powder metallurgical process of mechanical alloying (MA) and spark plasma sintering (SPS). MA process, microstructure, and mechanical properties of the WNbMoTaV alloy were studied systematically. During MA, a single *bcc* phase was formed and its mean particle size and crystallite size were estimated as 1.83 μm and 66.1 nm, respectively, after 6 h of MA.

In this communication, we report on the preparation of equiatomic HfTaTiNbZr-based refractory high-entropy alloy (RHEA) with a *bcc* structure by combined use of short-term high-energy ball milling and spark plasma sintering and on their structural and mechanical characterization.

2. Experimental

HfTaTiNbZr powder mixtures were prepared by two different pathways: (a) low-energy ball milling (LEBM) and (b) high-energy ball milling (HEBM) of the following elemental powder blends: Hf (99.1% pure, 100–200 μm), Ta (99.9%, 40–60 μm), Ti (99.2%, 40–60 μm), Nb (99.9% pure, 40–60 μm), and Zr (99.6%, 100–200 μm)—taken in equiatomic amounts. Mechanical treatment was performed in a water-cooled double-station planetary ball mill Activator-2s (Activator, Russia) using stainless-steel cylindrical jars and balls (5–7 mm in diameter). In all cases, the ball/powder ratio was 20:1 (by weight). The vial was evacuated and then filled with Ar gas at 4 atm. Ball milling was run at different rotation speeds of sun wheel/jars: 200/400 rpm (LEBM) and 694/1388 rpm (HEBM). Milling time (t) was varied between 20 and 90 min in the case of HEBM and between 1 and 10 h in the case of LEBM.

Starting and milled HfTaTiNbZr powder mixtures were SPS-consolidated in a vacuum in a Labox 650 facility (Sinter Land, Niigata, Japan). Powder mixture was placed into a cylindrical graphite die (inner diameter 15 mm) and uniaxially compressed at 50 MPa. Because one of HEA phases can be expected to exist at temperatures above 1020 $^{\circ}\text{C}$ [36], the sample was heated at a rate of 100 $^{\circ}\text{C}/\text{min}$ up to some preset sintering temperature in the range 1100–1700 $^{\circ}\text{C}$ by passing rectangular current pulses through the sample. The dwell time (τ) at sintering temperature was 10 min. SPS-produced disks were 2–3 mm thick and 15 mm in diameter.

Structure/composition of initial, milled, and consolidated powders were characterized by XRD (DRON-3M diffractometer, Saint Petersburg, Russia, Cu- K_{α} radiation, $2\theta = 20\text{--}95^{\circ}$), SEM (Vega 3 TESCAN, Brno, Czech Republic), and EDX (Oxford Inca spectrometer, Oxford, UK) using Aztec software. Microhardness was measured using an Emco-Test DuraScan 70 apparatus (Kuchl, Austria) under a load of 9.8 N. The thermal stability of initial and RHEA powder mixtures was studied by DSC (STA 449 F1 Simultaneous Thermal Analyzer, Netzsch, Germany) up to 1500 $^{\circ}\text{C}$ with a heating rate of 20 $^{\circ}\text{C}/\text{min}$ in an Ar atmosphere.

3. Results and Discussion

For predicting the formation of solid solutions in the HfTaTiNbZr system, we applied the well-established concepts of the HEA community [10] based on the Hume–Rothery rules, that is, taking into account composition-weighted terms for differences in atomic radii (Δr), electronegativity ($\Delta\chi$), and average valence electron concentration (VEC) and using the data presented in Table 1.

Table 1. Properties of the elements under consideration [8] (see the text for details). hcp, hexagonal closest packed; bcc, body-centered cubic; fcc, face-centered cubic; VEC, valence electron concentration; EN, electronegativity.

Elements	Atomic Number	Structure	Radius, pm	T_m (K)	VEC	Pauling EN
Hf	72	hcp	157.75	2233	4	1.30
Ta	73	bcc	143	3017	5	1.50
Ti	22	hcp	146.15	1670	4	1.54
Nb	41	bcc	142.9	2468	5	1.60
Zr	40	hcp	160.25	1851	4	1.33

It has been observed that the *bcc* and *fcc* phases in the system under study are formed for $VEC < 6.87$ and $VEC \geq 8.0$, respectively, while both phases (i.e., *bcc* + *fcc* mixture) coexist when $6.87 \leq VEC \leq 8.0$ [13].

For the HfTaTiNbZr composition, the atomic size difference ($\Delta r = 6.06\%$) is well within the adopted limits of $0 \leq \Delta r \leq 8.5\%$. $VEC = 4.4$ falls into the range for the formation of a *bcc* solid solution ($VEC < 6.87$) [13]. The electronegativity (EN) difference is 0.1445.

As known [12], electronegativity $\Delta\chi$ has little or no influence on the formation of solid-solution or amorphous phase. Even when no range has been prescribed for the formation of the disordered solid solution, it was noted [37] that a larger value of $\Delta\chi$ is expected to aid the formation of a compound. In our case, $\Delta\chi = 0.1176$.

In the present study, the following three approaches were applied: (a) SPS of elemental powders (Hf, Ta, Ti, Nb, Zr), (b) combination of LEBM and SPS, and (c) combination of HEBM and SPS.

3.1. SPS of Elemental Powders

Initial powder blends were prepared from elemental powders of Hf, Ta, Ti, Nb, and Zr taken in equatomic amounts and consolidated by SPS at different temperatures (1100 °C, 1300 °C, 1500 °C, and 1700 °C) in order to produce HfTaTiNbZr RHEA.

Before sintering, the blended powders exhibited diffraction lines from all of the constituent elements. SPS at 1100 °C is seen (Figure 1) to result in peaks' broadening, their overlapping, and the appearance of a signal at 33.56° corresponding to the Zr/Hf-based solid solution. The diffraction peaks from initial elements are still present in the XRD pattern.

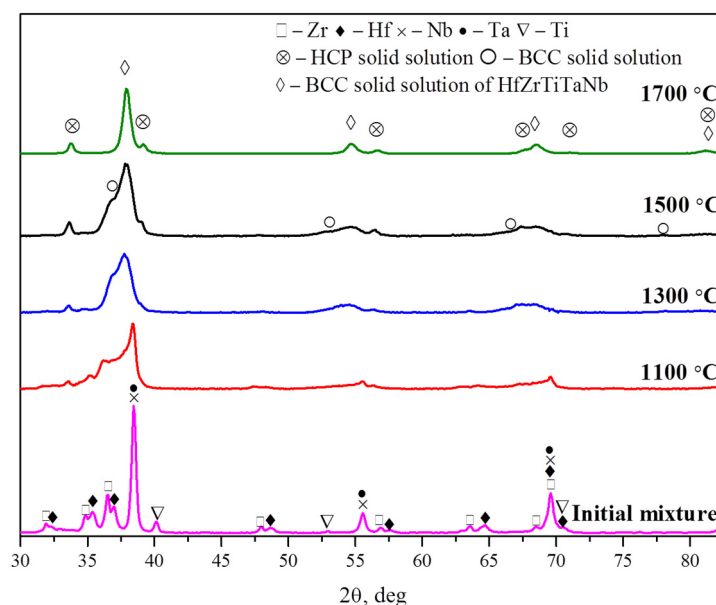


Figure 1. XRD patterns of initial HfTaTiNbZr powder blend and HfTaTiNbZr bulk specimens sintered at different temperatures (indicated). HCP, hexagonal closest packed; BCC, body-centered cubic.

On the basis of the SEM/EDX results (Figures 1 and 2), we may conclude that the formation of different solid solutions is due to material melting at grain boundaries. SPS at 1300 °C was found to yield *bcc* solid solution as a main phase. However, the presence of broad XRD peaks indicates the incomplete dissolution of metals. The diffraction pattern in Figure 2 also shows the presence of Hf- and Zr-based solid solutions.

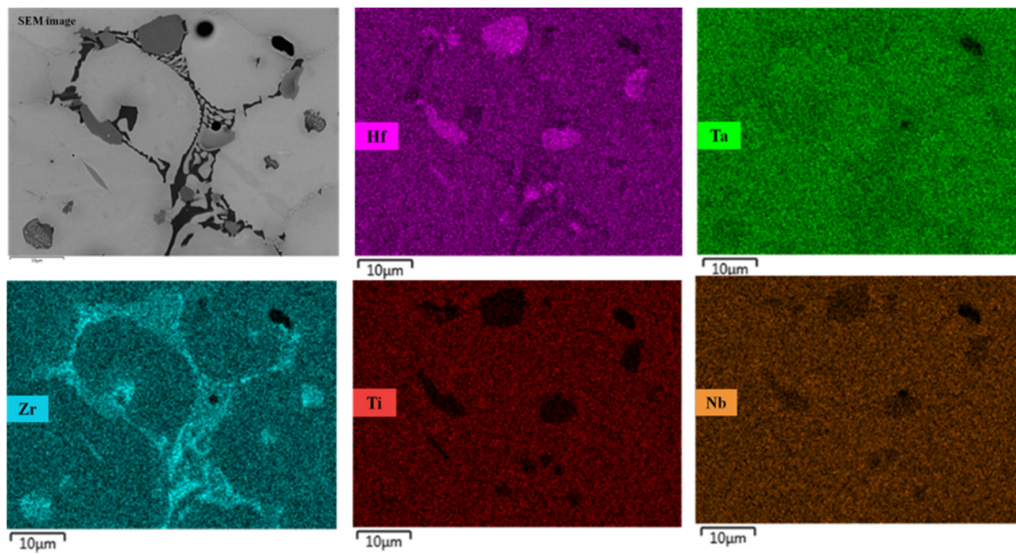


Figure 2. Representative compositional EDX mapping results for the HfTaTiNbZr sample consolidated at 1300 °C ($\tau = 0$ min).

The XRD results well agree with phase composition and EDX maps (Figure 2) for the HfTaTiNbZr sample consolidated at 1300 °C (dwell time 0 min). The principal elements are shown in color-scale contours. Pure Zr and Hf are still present in the bulk sample.

Upon SPS at 1500 °C, the crystallinity of the *bcc* phase grew, although the diffraction peaks from Zr and two solid solutions based on Zr and Hf (*hcp* with $a = 3.245$, $c = 5.140$ and *bcc* with $a = 3.455$) are still present in the form of lamellar inclusions on grain boundaries. Our XRD, SEM, and EDX results suggest that these phases are Hf- and Zr-based solid solutions with interlayers of Ta- and Nb-based solid solutions. Similar structures were observed in the HEAs prepared by arc remelting [38].

The final product sintered at 1700 °C was found to contain two solid solutions based on *bcc* and *hcp* phases. As the formation of *bcc* solid solution begins at 1300 °C, 10 min holding at 1300 °C was applied.

Figure 3 presents the XRD data and SEM images for the bulk HfTaTiNbZr specimens sintered at 1300 °C for 10 min and without dwell time ($\tau = 0$ min). After holding for 10 min, the crystallinity of the *bcc* and *hcp* phases increased: the XRD peaks become narrower. At the same time, the peak of Zr disappeared.

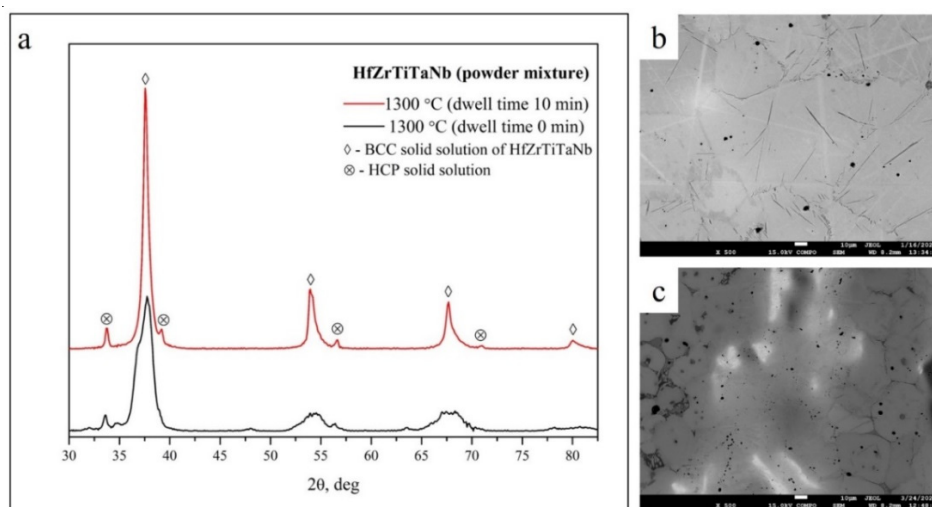


Figure 3. XRD patterns and SEM images of bulk HfTaTiNbZr specimens sintered at 1300 °C for $\tau = 10$ (a,b) and 0 min (a,c).

As follows from the data in Figures 3 and 4, the material obtained by SPS at 1300 °C for 10 min looks more dense (Figure 3b) and homogeneous (Figure 4) compared with that formed at $\tau = 0$ min (Figure 3c). The particles of Hf, Ta, Ti, Nb, and Zr are seen to be uniformly distributed over the material, although the traces of Hf-rich regions are still present on grain boundaries.

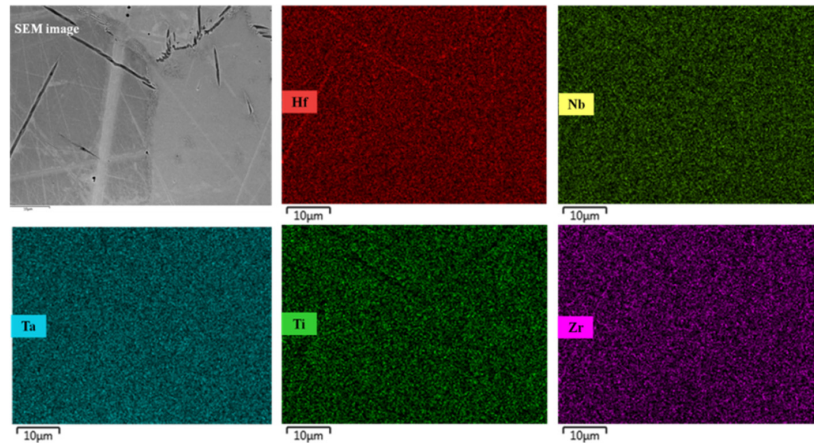


Figure 4. Representative compositional EDS mapping results for the HfTaTiNbZr sample consolidated at 1300 °C ($\tau = 10$ min).

As is known, the mechanical alloying (MA) process takes advantage of extended solid solubility even in immiscible systems [26]. In order to improve the solubility of solids in HfTaTiNbZr composition, we performed MA in two different modes, LEBM and HEBM.

3.2. Combined Use of LEBM and SPS

During LEBM (up to 10 h), the structure of milled HfTaTiNbZr powder blend underwent gradual changes, as illustrated in Figure 5.

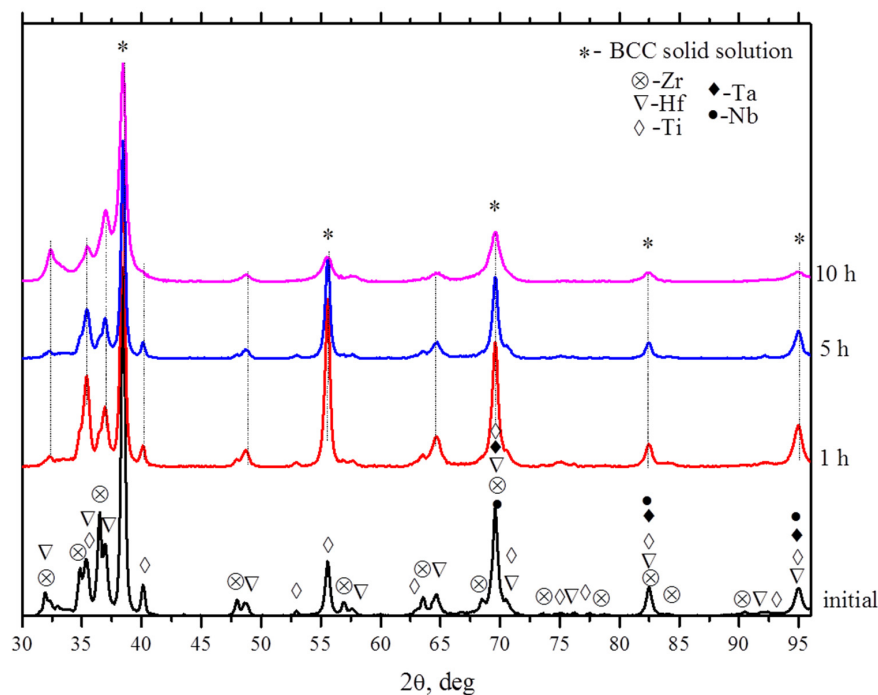


Figure 5. XRD patterns of HfTaTiNbZr powder mixtures taken after low-energy ball milling (LEBM) for different t (indicated on the right).

The initial HfTaTiNbZr powder blend exhibit expectedly strong and narrow Bragg peaks due to the crystalline structure of the elements. After 1 h of LEBM, the diffractions peaks of alloying elements broadened and decreased in their intensity. A further increase in milling time t up to 5 and 10 h leads to ongoing line broadening and partial overlapping of the main diffraction peaks from alloying elements. The formation of background around the (110), (200), (211), (220), and (310) peaks of the *bcc* phase is also observed. Most likely, this is caused by transformation of initially microcrystalline powders to nanocrystalline solid solutions and partial disordering of crystal structure upon mechanical damage.

Figures 6 and 7 show the representative compositional EDX mapping results for the HfTaTiNbZr sample ball milled for 5 and 10 h, respectively. In 5 h of LEBM, Hf, Ta, Ti, Nb, and Zr form separate agglomerates of layered structure (Figure 6), which is typical for ductile metal blends processed in a planetary ball mill [39]. Further mechanical treatment (Figure 7) leads to a decrease in the average layer thickness down to a nano scale. According to the EDX data, the non-uniform distribution of alloying elements is retained even after 10 h of LEBM.

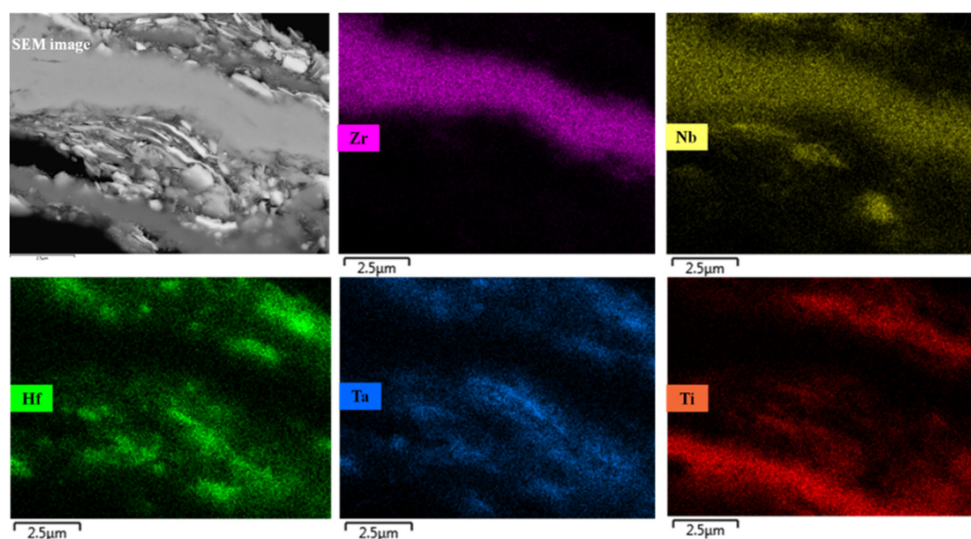


Figure 6. Representative compositional EDS mapping results for the HfTaTiNbZr sample ball milled for 5 h.

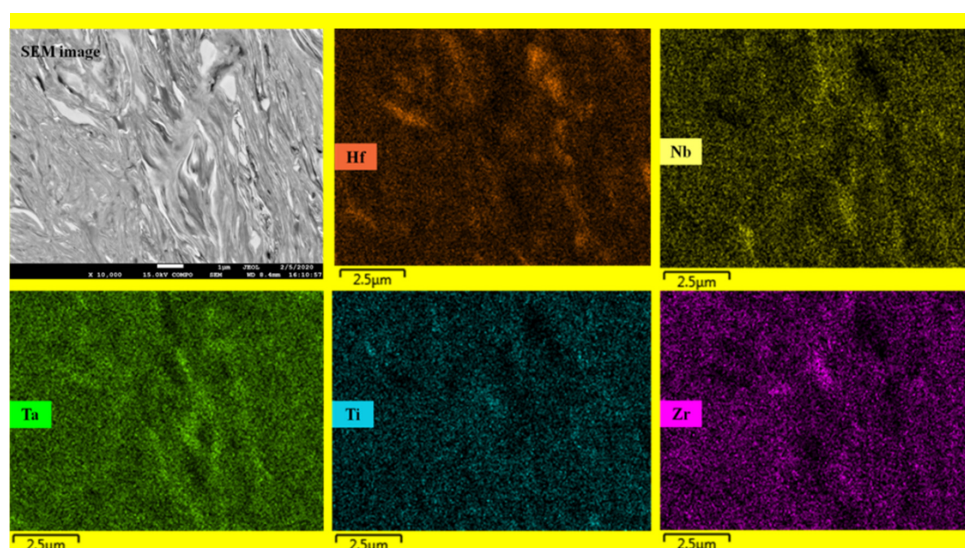


Figure 7. Representative compositional EDS mapping results for the HfTaTiNbZr sample ball milled for 10 h.

Figure 8 presents the XRD patterns and SEM images of LEBM-processed (10 h) HfTaTiNbZr specimens sintered at 1300 °C with dwell time $\tau = 10$ min (a,b) and $\tau = 0$ min (a). Just as in the case of the bulk HfTaTiNbZr materials derived from non-milled powder blends, consolidation of LEBM-processed nanocrystalline powder blend at 1300 °C for 10 min leads to an increase in the solubility of alloying metals and in the crystallinity of *bcc* and *hcp* phases.

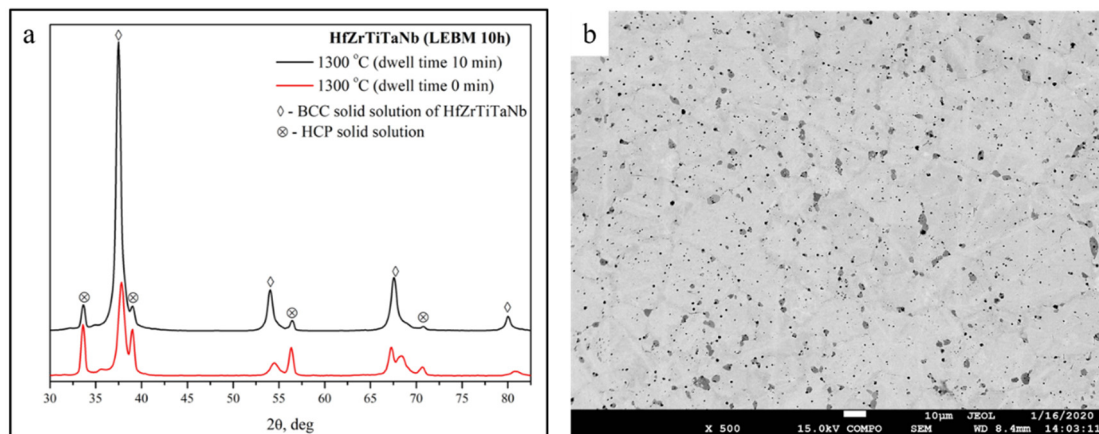


Figure 8. XRD patterns and SEM images of LEBM-processed (10 h) HfTaTiNbZr specimens sintered at 1300 °C with dwell time $\tau = 10$ min (a,b) and $\tau = 0$ min (a).

The EDX data suggest that the elemental distribution in the bulk HfTaTiNbZr material is most homogeneous, but contains some small Hf- and Zr-rich areas (cf. Figure 9).

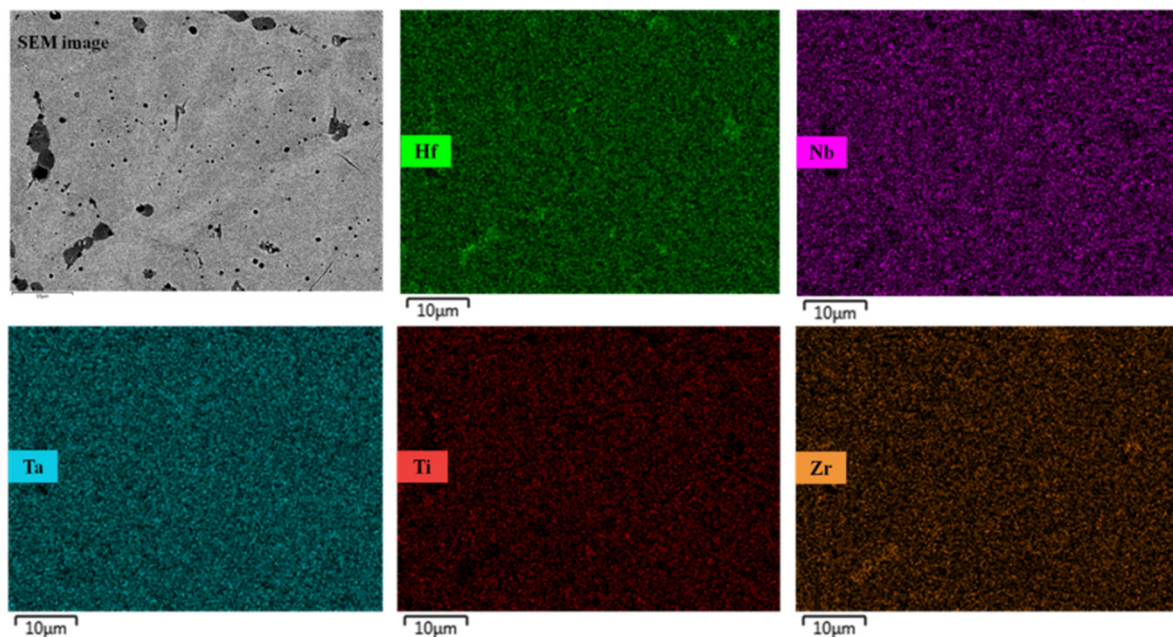


Figure 9. Representative compositional EDX mapping results for the HfTaTiNbZr sample consolidated at 1300 °C for 10 min after 10 h of LEBM.

On the basis of the above data, we can conclude that the use of LEBM has little or no positive influence on the structure of resultant HfTaTiNbZr alloys.

3.3. Combined Use of HEBM and SPS

HEBM processing of HfTaTiNbZr powder blends was found to bring about significant structural changes in their composition. Figure 10 shows the diffraction patterns taken after HEBM for different t (indicated). After 40 min of HEBM, the elemental Bragg peaks disappeared and the formation of solid solutions with a *hcp* (Hf-based) and *bcc* (Ta-based) structure began. Moreover, we observed the diffraction peak from the Fe that had been milled from steel drums and balls. Longer HEBM ($t > 60$ min) leads to the merging of the peaks from Hf-based (*hcp*) and Ta-based (*bcc*) solid solutions and the formation of a common asymmetric peak in the range $2\theta = 35\text{--}51^\circ$.

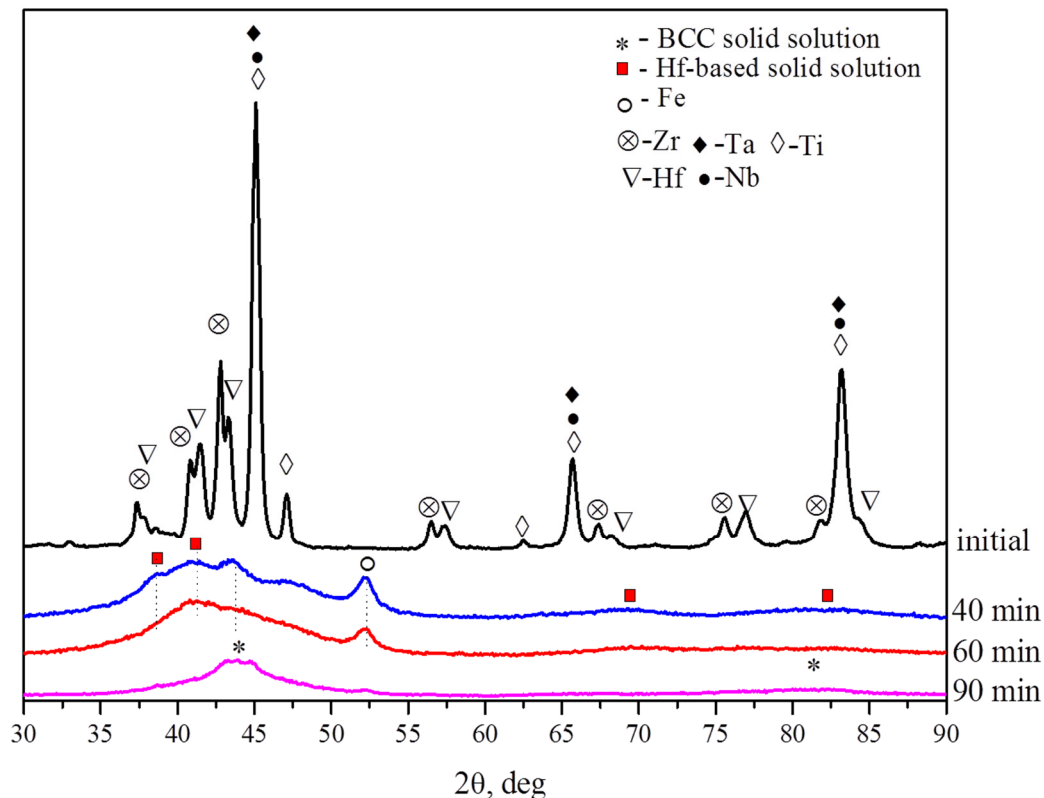


Figure 10. XRD patterns of HfTaTiNbZr powder mixtures taken after high-energy ball milling (HEBM) for different t (indicated on the right). The spectra are shifted along the y axis for the sake of clarity.

Signals from *bcc* HfTaTiNbZr solid solution (Figure 10) were detected after 90 min of HEBM. Note that the signal from Fe decreased slowly with increasing t , evidently to ever growing thickness of milled material on the surface of drums and balls during HEBM. In addition, some small amount of iron could partially dissolve in the *bcc* HfTaTiNbZr alloy.

The XRD pattern of RHEA alloy SPS consolidated at 1300°C , $\tau = 10$ min (Figure 11) clearly shows that the resultant material is comprised of three phases: (a) *bcc* HfZrTiTaNb solid solution (main phase); (b) *hcp* Hf- and Zr-based solid solution; and (c) a minor amount of the Me_2Fe phase, where $\text{Me} = \text{Hf, Zr}$.

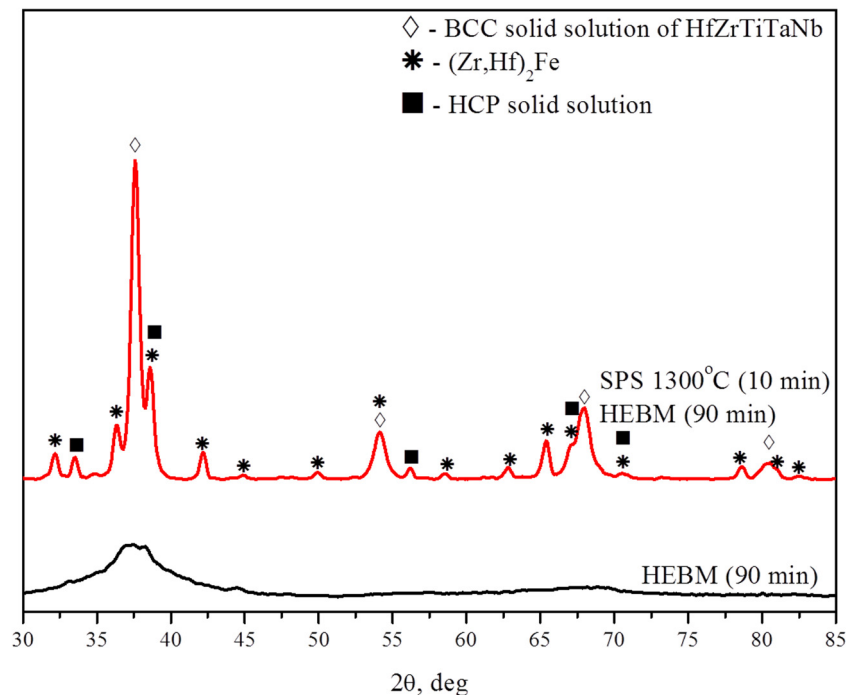


Figure 11. XRD patterns of HfTaTiNbZr powder after HEBM for $t = 90$ min (lower curve) and of bulk sample sintered at $1300\text{ }^{\circ}\text{C}$ for $\tau = 10$ min. SPS, spark plasma sintering.

The presence of $(\text{Hf}, \text{Zr})_2\text{Fe}$ may affect the physicochemical parameters of HEAs such as electronic behavior, electrical conductivity, magnetic properties, and hydrogen sorption/desorption kinetics [40,41]. Our multicomponent composite can be recommended not only for structural applications, but also as a material for hydrogen storage [42].

Figure 12 shows the SEM image and EDX mapping results for the bulk HfTaTiNbZr sample ($t = 90$ min, SPS at $1300\text{ }^{\circ}\text{C}$, $\tau = 10$ min), illustrating uniform distribution of the principal elements.

Therefore, it turns out that SPS-produced alloys always contain the inclusions of Hf- and Zr-based solid solutions. In the absence of MA and in the case of LEBM, this can happen by the following scheme. During warmup, *hcp* and *bcc* metals form two solutions. At some temperature T , the *hcp* lattice undergoes transformation into a *bcc* one, which is followed by (a) mutual inter-dissolution of Ta- and Nb-based alloys and (b) formation of Ta/Nb-based and Hf/Zr-based HEAs. In the case of $\tau = 0$, the inter-dissolution remains incomplete and the resultant material exhibits the presence of inclusions and respective diffraction lines (cf. Figures 3 and 4c). Such a scheme is also supported by a more uniform structure of materials sintered at higher T or longer dwell time.

In the case of HEBM, the resultant materials turn uniform. Thermodynamics predicts that our alloy is non-equilibrium at temperatures below $800\text{ }^{\circ}\text{C}$. In view of this, during heating, it decomposes into the following three phases: one *bcc* Ta/Nb phase and two Hf/Zr-based phases. A high amount of structural defects acquired during the MA non-equilibrium nature of the phases favors the formation of numerous Hf-/Zr-based inclusions.

The LEBM or HEBM powders sintered below $1300\text{ }^{\circ}\text{C}$ showed the presence of rounded inclusions because of incomplete dissolution during the formation of the RHEA phase. In the case of non-milled powder blends, the formation of needle-like and lamellar inclusions on the grain boundaries was observed.

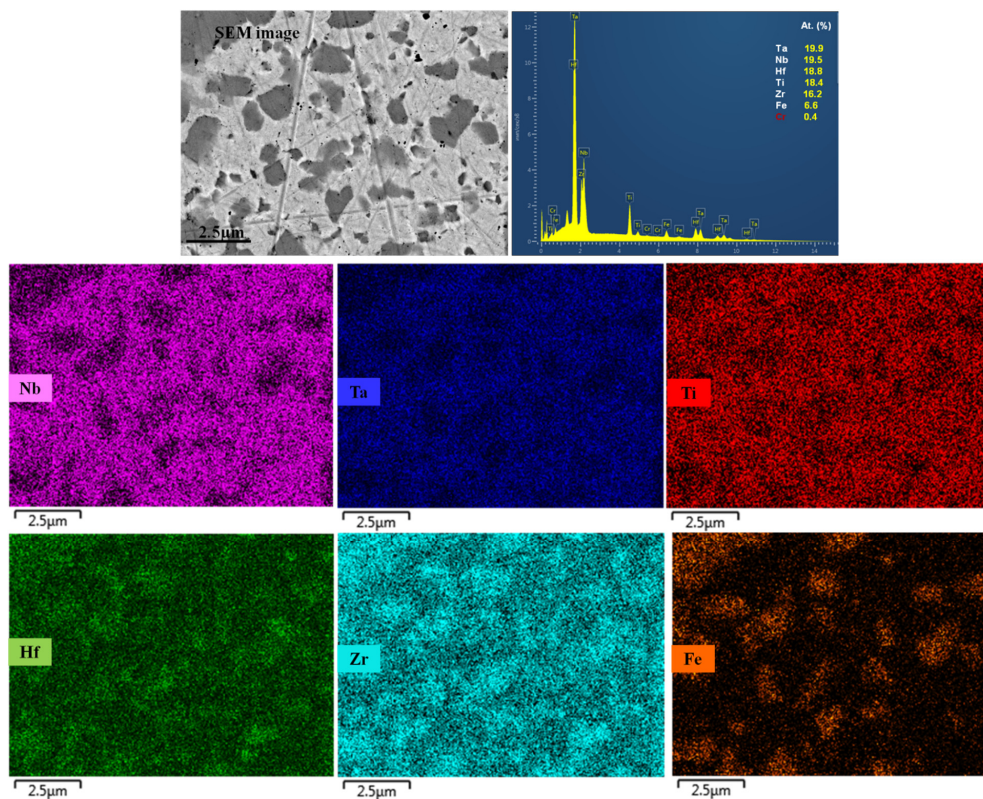


Figure 12. Representative compositional EDX mapping results for the HfTaTiNbZr sample prepared by the combined use of HEBM ($t = 90$ min) and SPS consolidation at 1300 °C ($\tau = 10$ min).

The DSC curves for initial (curve 1), LEBM (curve 2), and HEBM (curve 3) HfZrTiTaNb powders are presented in Figure 13a. DSC curves 1 and 2 exhibit two low-exothermic peaks around 350 °C and 700 °C for LEBM powders and around 350 °C and 620 °C for HEBM powders, respectively.

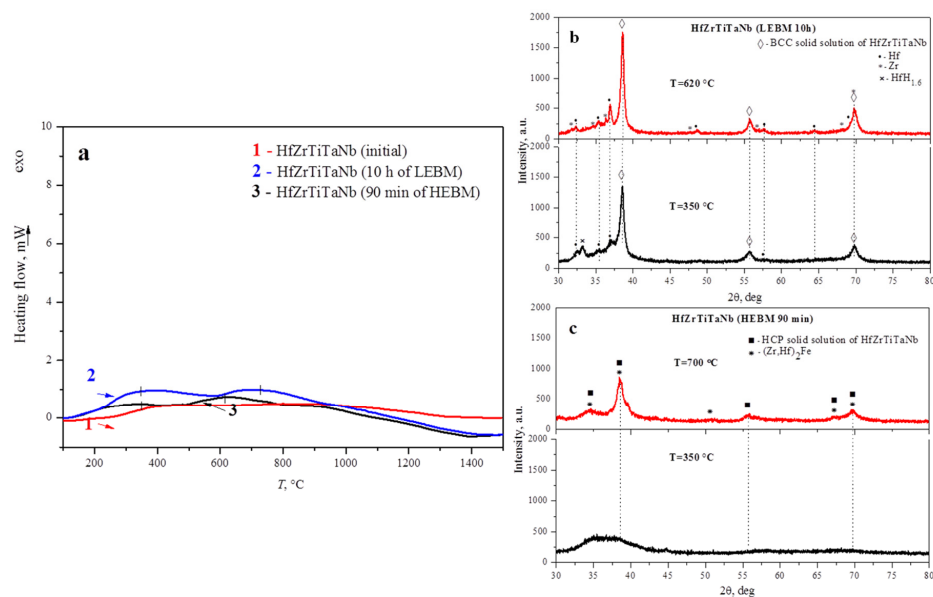


Figure 13. (a) DSC curves for HfZrTiTaNb powders: (1) initial, (2) after 90 min of HEBM, and (3) after 10 h of LEBM; (b) XRD patterns of LEBM-processed HfTaTiNbZr powder mixtures at 350 °C and 620 °C; and (c) XRD patterns of HEBM-processed HfTaTiNbZr powder mixtures at 350 °C and 700 °C.

On the basis of the XRD results for LEBM (Figure 13b) and HEBM (Figure 13c) powders, we may conclude that the thermal effects at 320 °C and 350 °C have nothing in common with phase transformations, but can be associated with partial oxidation by traces of oxygen in the calorimeter. Exothermic peaks at 700 °C for LEBM powders and at 620 °C for HEBM powders correspond to partial crystallization. The XRD peaks of *bcc* phase become narrower and stronger.

No doubt, the understanding of the phases' formation and their stability as a function of time in RHEA HfTaTiNbZr materials deserve further detailed investigation.

The Vickers hardness of RHEA materials prepared by HEBM ($t = 90$ min) and SPS consolidation (1300 °C, $\tau = 10$ min) turned markedly higher (10.7 GPa) than that of SPS-produced from unprocessed elemental powders (6.4 GPa) or from LEBM ($t = 10$ h) powders (5.8 GPa). Moreover, this is the highest value of Vickers hardness of all HEAs listed in [43] and three times higher than that for the HfTaTiNbZr alloy prepared by arc melting [24]. The density of our HfTaTiNbZr alloy is 9.87 ± 0.18 g/cm³ (98.7%). Superhigh hardness of our alloy can be associated with the strengthening of (a) solid solution caused by strong lattice distortion [10] and (b) grain boundaries with ultrafine grains. A similar increase in mechanical properties was reported for SPSed WNbMoTaV [44].

4. Conclusions

(1) Powder of refractory *bcc* HfTaTiNbZr-based high-entropy alloy (RHEA) was successfully produced by short-term (90 min) HEBM. The evolution in the structure of initial HfTaTiNbZr powder mixture during HEBM was elucidated by XRD. All Bragg peaks of principal elements, intermediate solid solutions with a *hcp* (Hf-based) and *bcc* (Ta-based) structure, vanished in 90 min of HEBM, forming HEA solid solution with a *bcc* structure.

(2) Consolidation of HEBM-produced RHEA powder by SPS at 1300 °C for 10 min results in the formation of bulk material with an ultra-high Vickers hardness (10.7 GPa) and a density of 9.87 ± 0.18 g/cm³ (98.7%).

(3) On the basis of the XRD and SEM/EDX results, HfTaTiNbZr-based RHEA alloy was found to consist of *bcc* HfZrTiTaNb as a main phase, *hcp* Hf/Zr-based solid solution, and Me₂Fe phases (Me = Hf, Zr) as minor admixtures. Principal elements of the HEA phase were uniformly distributed over the bulk of HfTaTiNbZr alloy.

(4) The HfTaTiNbZr alloys synthesized in the absence of ball milling and in the case of low-energy ball milling (LEBM, 10 h) consisted of *bcc* HEA and Hf/Zr-rich *hcp* solid solution; in this case, the Vickers hardness of such alloys was found to have a value of 6.4 GPa and 5.8 GPa, respectively.

(5) An optimal combination of HEBM and SPS processes can be recommended as a facile route for fabrication of equiatomic refractory HfTaTiNbZr-based high-entropy powders and bulk materials with the best structural/elemental homogeneity and promising mechanical properties.

Author Contributions: A.S., S.B., and D.M. conceived of and designed the experiments. A.S., S.B., S.V., and K.K. performed the experiments. N.S., K.K., Y.S., and D.M. analyzed the data and wrote the paper. All authors have read and agreed to the published version of the manuscript.

Funding: This research was funded by the Russian Science Foundation, Grant Number 18-79-10215.

Acknowledgments: This work was conducted with the financial support of the Russian Science Foundation (Grant Number 18-79-10215).

Conflicts of Interest: The authors declare no conflict of interest.

References

1. Yeh, J.-W.; Chen, S.-K.; Lin, S.-J.; Gan, J.-Y.; Chin, T.-S.; Shun, T.-T.; Tsau, C.-H.; Chang, S.-Y. Nanostructured High-Entropy Alloys with Multiple Principal Elements: Novel Alloy Design Concepts and Outcomes. *Adv. Eng. Mater.* **2004**, *6*, 299–303. [[CrossRef](#)]
2. Cantor, B.; Chang, I.T.H.; Knight, P.; Vincent, A.J.B. Microstructural development in equiatomic multicomponent alloys. *Mater. Sci. Eng. A* **2004**, *375–377*, 213–218. [[CrossRef](#)]

3. Gludovatz, B.; Hohenwarter, A.; Catoor, D.; Chang, E.H.; George, E.P.; Ritchie, R.O. A fracture-resistant high-entropy alloy for cryogenic applications. *Science* **2014**, *345*, 1153–1158. [[CrossRef](#)] [[PubMed](#)]
4. Zhang, Z.; Mao, M.M.; Wang, J.; Gludovatz, B.; Zhang, Z.; Mao, S.X.; George, E.P.; Yu, Q.; Ritchie, R.O. Nanoscale origins of the damage tolerance of the high-entropy alloy CrMnFeCoNi. *Nat. Commun.* **2015**, *6*, 10143. [[CrossRef](#)] [[PubMed](#)]
5. Gali, A.; George, E.P. Tensile properties of high- and medium-entropy alloys. *Intermetallics* **2013**, *39*, 74–78. [[CrossRef](#)]
6. Otto, F.; Dlouhý, A.; Somsen, C.; Bei, H.; Eggeler, G.; George, E.P. The influences of temperature and microstructure on the tensile properties of a CoCrFeMnNi high-entropy alloy. *Acta Mater.* **2013**, *61*, 5743–5755. [[CrossRef](#)]
7. Kilmametov, A.; Kulagin, R.; Mazilkin, A.; Seils, S.; Boll, T.; Heilmaier, M.; Hahn, H. High-pressure torsion driven mechanical alloying of CoCrFeMnNi high entropy alloy. *Scr. Mater.* **2019**, *158*, 29–33. [[CrossRef](#)]
8. Zhu, C.; Lu, Z.P.; Nieh, T.G. Incipient plasticity and dislocation nucleation of FeCoCrNiMn high-entropy alloy. *Acta Mater.* **2013**, *61*, 2993–3001. [[CrossRef](#)]
9. Sun, S.J.; Tian, Y.Z.; Lin, H.R.; Dong, X.G.; Wang, Y.H.; Zhang, Z.J.; Zhang, Z.F. Enhanced strength and ductility of bulk CoCrFeMnNi high entropy alloy having fully recrystallized ultrafine-grained structure. *Mater. Des.* **2017**, *133*, 122–127. [[CrossRef](#)]
10. Miracle, D.B.; Senkov, O.N. A critical review of high entropy alloys and related concepts. *Acta Mater.* **2017**, *122*, 448–511. [[CrossRef](#)]
11. Chang, X.; Zeng, M.; Liu, K.; Fu, L. Phase Engineering of High-Entropy Alloys. *Adv. Mater.* **2020**, *32*, 1907226. [[CrossRef](#)] [[PubMed](#)]
12. GUO, S.; LIU, C.T. Phase stability in high entropy alloys: Formation of solid-solution phase or amorphous phase. *Prog. Nat. Sci. Mater. Int.* **2011**, *21*, 433–446. [[CrossRef](#)]
13. Guo, S.; Ng, C.; Lu, J.; Liu, C.T. Effect of valence electron concentration on stability of fcc or bcc phase in high entropy alloys. *J. Appl. Phys.* **2011**, *109*, 103505. [[CrossRef](#)]
14. Mishra, R.K.; Shahi, R.R. Magnetic Characteristics of High Entropy Alloys. In *Magnetism and Magnetic Materials*; InTech: London, UK, 2018.
15. Zhang, K.; Fu, Z. Effects of annealing treatment on phase composition and microstructure of CoCrFeNiTiAlx high-entropy alloys. *Intermetallics* **2012**, *22*, 24–32. [[CrossRef](#)]
16. Zhrebtsov, S.; Stepanov, N.; Ivanisenko, Y.; Shaysultanov, D.; Yurchenko, N.; Klimova, M.; Salishchev, G. Evolution of Microstructure and Mechanical Properties of a CoCrFeMnNi High-Entropy Alloy during High-Pressure Torsion at Room and Cryogenic Temperatures. *Metals (Basel)* **2018**, *8*, 123. [[CrossRef](#)]
17. Rogachev, A.S.; Vadchenko, S.G.; Kochetov, N.A.; Rouvimov, S.; Kovalev, D.Y.; Shchukin, A.S.; Moskovskikh, D.O.; Nepapushev, A.A.; Mukasyan, A.S. Structure and properties of equiatomic CoCrFeNiMn alloy fabricated by high-energy ball milling and spark plasma sintering. *J. Alloys Compd.* **2019**, *805*, 1237–1245. [[CrossRef](#)]
18. Wang, H.; Gao, T.; Niu, J.; Shi, P.; Xu, J.; Wang, Y. Microstructure, thermal properties, and corrosion behaviors of FeSiBAlNi alloy fabricated by mechanical alloying and spark plasma sintering. *Int. J. Miner. Metall. Mater.* **2016**, *23*, 77–82. [[CrossRef](#)]
19. Murty, B.S.; Yeh, J.-W.; Ranganathan, S.; Bhattacharjee, P.P. *High-Entropy Alloys*; Elsevier: London, UK, 2019; ISBN 9780128160671.
20. Gao, M.C.; Yeh, J.-W.; Liaw, P.K.; Zhang, Y. *High-Entropy Alloys Fundamentals and Applications*; Gao, M.C., Yeh, J.-W., Liaw, P.K., Zhang, Y., Eds.; Springer International Publishing: Cham, Switzerland, 2016; ISBN 978-3-319-27011-1.
21. Syed Ghazi, S.; Ravi, K.R. Phase-evolution in high entropy alloys: Role of synthesis route. *Intermetallics* **2016**, *73*, 40–42. [[CrossRef](#)]
22. Panina, E.; Yurchenko, N.; Zhrebtsov, S.; Stepanov, N.; Salishchev, G.; Ventzke, V.; Dinse, R.; Kashaev, N. Laser Beam Welding of a Low Density Refractory High Entropy Alloy. *Metals (Basel)* **2019**, *9*, 1351. [[CrossRef](#)]
23. Yurchenko, N.; Panina, E.; Zhrebtsov, S.; Salishchev, G.; Stepanov, N. Oxidation Behavior of Refractory AlNbTiVZr0.25 High-Entropy Alloy. *Materials (Basel)* **2018**, *11*, 2526. [[CrossRef](#)]
24. Senkov, O.N.; Scott, J.M.; Senkova, S.V.; Miracle, D.B.; Woodward, C.F. Microstructure and room temperature properties of a high-entropy TaNbHfZrTi alloy. *J. Alloys Compd.* **2011**, *509*, 6043–6048. [[CrossRef](#)]

25. Liu, Q.; Wang, G.; Sui, X.; Liu, Y.; Li, X.; Yang, J. Microstructure and mechanical properties of ultra-fine grained MoNbTaTiV refractory high-entropy alloy fabricated by spark plasma sintering. *J. Mater. Sci. Technol.* **2019**, *35*, 2600–2607. [[CrossRef](#)]
26. Shkodich, N.F.; Rogachev, A.S.; Vadchenko, S.G.; Moskovskikh, D.O.; Sachkova, N.V.; Rouvimov, S.; Mukasyan, A.S. Bulk Cu-Cr nanocomposites by high-energy ball milling and spark plasma sintering. *J. Alloys Compd.* **2014**, *617*, 39–46. [[CrossRef](#)]
27. Murty, B.S.; Ranganathan, S. Novel materials synthesis by mechanical alloying/milling. *Int. Mater. Rev.* **1998**, *43*, 101–141. [[CrossRef](#)]
28. Shkodich, N.F.; Vadchenko, S.G.; Nepapushev, A.A.; Kovalev, D.Y.; Kovalev, I.D.; Ruvimov, S.; Rogachev, A.S.; Mukasyan, A.S. Crystallization of amorphous Cu₅₀Ti₅₀ alloy prepared by high-energy ball milling. *J. Alloys Compd.* **2018**, *741*, 575–579. [[CrossRef](#)]
29. Rogachev, A.S. Mechanical activation of heterogeneous exothermic reactions in powder mixtures. *Russ. Chem. Rev.* **2019**, *88*, 875–900. [[CrossRef](#)]
30. Rogachev, A.S.; Kuskov, K.V.; Moskovskikh, D.O.; Usenko, A.A.; Orlov, A.O.; Shkodich, N.F.; Alymov, M.I.; Mukasyan, A.S. Effect of mechanical activation on thermal and electrical conductivity of sintered Cu, Cr, and Cu/Cr composite powders. *Dokl. Phys.* **2016**, *61*. [[CrossRef](#)]
31. Varalakshmi, S.; Kamaraj, M.; Murty, B.S. Synthesis and characterization of nanocrystalline AlFeTiCrZnCu high entropy solid solution by mechanical alloying. *J. Alloys Compd.* **2008**, *460*, 253–257. [[CrossRef](#)]
32. Cavaliere, P.; Sadeghi, B.; Shabani, A. Spark Plasma Sintering: Process Fundamentals. In *Spark Plasma Sintering of Materials: Advances in Processing and Applications*; Springer Nature: Basel, Switzerland, 2019; ISBN 9783030053277.
33. Hu, Z.-Y.; Zhang, Z.-H.; Cheng, X.-W.; Wang, F.-C.; Zhang, Y.-F.; Li, S.-L. A review of multi-physical fields induced phenomena and effects in spark plasma sintering: Fundamentals and applications. *Mater. Des.* **2020**, 108662. [[CrossRef](#)]
34. Dudina, D.V.; Bokhonov, B.B.; Olevsky, E.A. Fabrication of porous materials by spark plasma sintering: A review. *Materials (Basel)* **2019**, *12*, 541. [[CrossRef](#)]
35. Abedi, M.; Moskovskikh, D.O.; Rogachev, A.S.; Mukasyan, A.S. Spark Plasma Sintering of Titanium Spherical Particles. *Metall. Mater. Trans. B Process Metall. Mater. Process. Sci.* **2016**, *47*. [[CrossRef](#)]
36. Schuh, B.; Völker, B.; Todt, J.; Schell, N.; Perrière, L.; Li, J.; Couzinié, J.P.; Hohenwarter, A. Thermodynamic instability of a nanocrystalline, single-phase TiZrNbHfTa alloy and its impact on the mechanical properties. *Acta Mater.* **2018**, *142*, 201–212. [[CrossRef](#)]
37. Singh, A.K.; Subramaniam, A. On the formation of disordered solid solutions in multi-component alloys. *J. Alloys Compd.* **2014**, *587*, 113–119. [[CrossRef](#)]
38. Chen, S.Y.; Tong, Y.; Tseng, K.-K.; Yeh, J.-W.; Poplawsky, J.D.; Wen, J.G.; Gao, M.C.; Kim, G.; Chen, W.; Ren, Y.; et al. Phase transformations of HfNbTaTiZr high-entropy alloy at intermediate temperatures. *Scr. Mater.* **2019**, *158*, 50–56. [[CrossRef](#)]
39. Rogachev, A.S.; Shkodich, N.F.; Vadchenko, S.G.; Baras, F.; Kovalev, D.Y.; Rouvimov, S.; Nepapushev, A.A.; Mukasyan, A.S. Influence of the high energy ball milling on structure and reactivity of the Ni + Al powder mixture. *J. Alloys Compd.* **2013**, *577*, 600–605. [[CrossRef](#)]
40. Martinez-Amariz, A.; Peña, D.; Montes Vera, E. Metal hydrides with body-centered cubic structure: Advantages and challenges. *J. Phys. Conf. Ser.* **2019**, *1386*, 012061. [[CrossRef](#)]
41. Zavaliy, I.Y.; Riabov, A.; Yartys, V.; Wiesinger, G.; Michor, H.; Hilscher, G. (Hf,Zr)₂Fe and Zr₄Fe₂O_{0.6} compounds and their hydrides: Phase equilibria, crystal structure and magnetic properties. *J. Alloys Compd.* **1998**, *265*, 6–14. [[CrossRef](#)]
42. Zadorozhnyy, V.; Sarac, B.; Berdonosova, E.; Karazehir, T.; Lassnig, A.; Gammer, C.; Zadorozhnyy, M.; Ketov, S.; Klyamkin, S.; Eckert, J. Evaluation of hydrogen storage performance of ZrTiVNiCrFe in electrochemical and gas-solid reactions. *Int. J. Hydrogen Energy* **2020**, *45*, 5347–5355. [[CrossRef](#)]

43. Gorsse, S.; Nguyen, M.H.; Senkov, O.N.; Miracle, D.B. Database on the mechanical properties of high entropy alloys and complex concentrated alloys. *Data Br.* **2018**, *21*, 2664–2678. [[CrossRef](#)]
44. Kang, B.; Lee, J.; Ryu, H.J.; Hong, S.H. Ultra-high strength WNbMoTaV high-entropy alloys with fine grain structure fabricated by powder metallurgical process. *Mater. Sci. Eng. A* **2018**, *712*, 616–624. [[CrossRef](#)]



© 2020 by the authors. Licensee MDPI, Basel, Switzerland. This article is an open access article distributed under the terms and conditions of the Creative Commons Attribution (CC BY) license (<http://creativecommons.org/licenses/by/4.0/>).